Coupling Light to The Transverse Modes of a Near-Concentric Optical Cavity

ADRIAN NUGRAHA UTAMA,[1] CHANG HOONG CHOW,[1], CHI HUAN NGUYEN,[1] AND CHRISTIAN KURTSIEFER[1,2,*]

[1]*Centre for Quantum Technologies, 3 Science Drive 2, Singapore 117543*
[2]*Department of Physics, National University of Singapore, 2 Science Drive 3, Singapore 117542*
[*]*phyck@nus.edu.sg*

Abstract: Optical cavities in the near-concentric regime have near-degenerate transverse modes. The tight focusing transverse modes in this regime enable strong coupling with atoms. These features provide an interesting platform to explore multi-mode interaction between atoms and light. Here, we use a phase spatial light modulator (SLM) to shape the incoming light and match the Laguerre-Gaussian (LG) modes of a near-concentric optical cavity. We demonstrate coupling efficiency close to the theoretical prediction for single LG modes and combinations of them, limited mainly by imperfections in the cavity alignment.

1. Introduction

Transverse modes constitute a separate degree of freedom, apart from frequency, wavevector and polarization, in the propagation of electromagnetic waves. It has a wide range of applications, such as increasing the information-carrying capacity in free-space [1] and fiber [2, 3] communications, creating smaller focal volumes to achieve superresolution imaging [4], utilizing orbital angular momentum (OAM) to perform quantum key distribution [5], and producing highly-entangled OAM states [6]. One particular area where transverse modes has garnered substantial interest is in optical cavities. For example, transverse modes can be used to track atomic position via the observed mode pattern [7–9]. They can also exhibit inter-mode coupling in the near-degenerate configuration [10, 11], and help enhancing the cooling process in atomic ensembles [12–14]. Perhaps the most exotic application of multiple near-degenerate transverse modes (multimode) cavities is in Bose-Einstein condensates (BEC), where they are used to engineer the atomic interaction within the BEC to create regions of crystallized domains [15–18].

Optical cavities in the near-concentric regime produce highly focused mode with diffraction-limited focal spot, which enable strong interaction between the optical mode and the atoms placed within [19–21]. Similar to confocal cavities [16, 22], the transverse mode frequencies of the concentric cavities overlap at the critical point. Even though the critical point is only marginally stable, the cavity can support the fundamental mode less than a wavelength away from the critical point [23]. In the near-concentric regime, the frequency spacing of the transverse modes can be engineered to be ~ 0.01 to ~ 1 GHz, which are on the order of the hyperfine splitting or the magnetic levels of the atoms. This provides an alternative system to explore atomic nonlinearities with multiple modes simultaneously [24] and extend it to various atomic energy levels and spatial distributions via the transverse modes.

In this work, we couple light selectively to the transverse modes of a near-concentric cavity, characterize their mode structures, and optimize the efficiencies of the coupling procedure. To prepare light from a collimated fiber output to match the spatial distribution of the cavity transverse modes, we use a liquid crystal spatial light modulator (SLM), which modifies the spatial phase information of the incoming beam [25]. In previous works, SLMs have been utilized to excite transverse modes of an optical channel: in multimode fibers with a phase SLM [26] and in confocal cavities using a digital micromirror device [22] – to the best of our knowledge, it

has not been done in near-concentric cavities which may exhibit more technical complexities. Furthermore, we extend this mode-matching procedure to generate a superposition of the modes and obtain the efficiency. We show that the efficiency depends on the relative phases of the modes. Finally, we examine how close to the critical point are the transverse modes still supported.

2. Theory

2.1. Transverse modes of a cavity

Optical modes of a cylindrically symmetric cavity with spherical mirrors can be described by the standing wave of the Laguerre-Gaussian (LG) beam [27]:

$$U_{m,l}(\rho,\phi,z) = A_{l,m}\frac{w_0}{w(z)}\left(\frac{\rho}{w(z)}\right)^l \mathcal{L}_m^l\left(\frac{2\rho^2}{w^2(z)}\right)\exp\left(-\frac{\rho^2}{w^2(z)}\right)\exp\left(i\,\psi_{m,l}(\rho,\phi,z)\right)\,, \quad (1)$$

where m and l are the radial and azimuthal mode numbers of the LG beams, $A_{l,m}$ is the normalization constant, $w(z) = w_0\sqrt{1+(z/z_0)^2}$ is the beam radius with $z_0 = \pi w_0^2/\lambda$ as the Rayleigh range, $\mathcal{L}_m^l(.)$ is the generalized Laguerre polynomial function, and $\psi_{m,l}(\rho,\phi,z)$ is the real-valued phase of the LG beam, given by:

$$\psi_{m,l}(\rho,\phi,z) = -kz - k\frac{\rho^2}{2R(z)} - l\phi + (2m+l+1)\zeta(z)\,, \quad (2)$$

where $R(z) = z + z_0^2/z$ is the radius of the wavefront and $\zeta(z) = \tan^{-1}(z/z_0)$ is the Gouy phase.

Inside a cavity, the LG modes are bounded by the two mirrors of radii R_1 and R_2 spaced L apart. The g-parameters, $g_1 = 1 - L/R_1$ and $g_2 = 1 - L/R_2$ specify the geometry and stability of the cavity mode. In symmetric cavities ($g_1 = g_2 = g$), the concentric mode is obtained when $L = 2R$ and $g = -1$ (critical point) and is only marginally stable. Near-concentric cavity modes depart from this critical point towards the stable region – we define this distance as the critical distance $d = 2R - L$, with $g = -1 + d/R$.

The resonance frequencies of the cavity depend on the transverse mode numbers m and l:

$$\nu_{q,m,l} = \nu_F\left(q + (2m+l+1)\frac{\Delta\zeta}{\pi}\right) \quad (3)$$

where q is the longitudinal mode number of the cavity, $\nu_F = c/2L$ is the cavity free spectral range, and $\Delta\zeta = \zeta(z_{M2}) - \zeta(z_{M1})$ is the Gouy phase difference between the two cavity mirrors. In near-concentric symmetrical cavities, the transverse mode spacing is given by

$$\Delta\nu_{tr} = \nu_{q+1,0,0} - \nu_{q,0,1} = \frac{\nu_F}{\pi}\cos^{-1}\left(1 - \frac{d}{R}\right)\,, \quad (4)$$

where $\Delta\nu_{tr} \to 0$ as $d \to 0$. The critical distance d can thus be estimated by measuring the frequency separation between the transverse modes [23].

Near-concentric cavities produce atom-cavity coupling strength $g_{ac} \propto 1/\sqrt{V_m}$ comparable to μm-length cavities or microcavities [21], as the effective mode volume $V_m \approx \pi W_0^2 L$ decreases in tighter focal radii W_0. Interestingly, all the radial modes (transverse modes with $l = 0$) at a particular critical distance has identical effective mode volumes, resulting in coupling strengths which are equally strong across all radial modes. This comes from the normalization relation $\int_0^\infty e^{-u}\left[\mathbb{L}_m^0(u)\right]^2 du = 1$, yielding the same prefactor $A_{0,m}$ for all radial modes in Eq. 1.

2.2. Mode matching to a cavity

The power transmission through a cavity with identical mirrors is given by [28]:

$$T(\omega) = \frac{P_t(\omega)}{P_{in}} = \eta \frac{\kappa_m^2}{(\kappa_m + \kappa_l)^2 + (\omega - \omega_0)^2} , \tag{5}$$

where $P_t(\omega)$ is the light power transmitted through the cavity, P_{in} is the input power, η is the spatial mode matching efficiency, ω_0 is the cavity resonance frequency, and κ_m and κ_l are the cavity decay rates due to the mirror transmission and scattering losses, respectively. On the other hand, the power reflection of the cavity is given by

$$R(\omega) = \frac{P_r(\omega)}{P_{in}} = 1 - \eta \frac{\kappa_m^2 + 2\kappa_m\kappa_l}{(\kappa_m + \kappa_l)^2 + (\omega - \omega_0)^2} , \tag{6}$$

where $P_r(\omega)$ is the light power reflected by the cavity. The finesse of the cavity is given by $F = \pi/\kappa v_F$, where $\kappa = \kappa_m + \kappa_l$ is the total cavity decay rate, obtained from fitting Eq. (5) to the transmission spectrum.

From the transmission and reflection spectrum, the spatial mode matching efficiency η can be obtained. First, we define the "effective" transmission coefficient

$$\alpha = \frac{T(\omega_0)}{1 - R(\omega_0)} , \tag{7}$$

where T and R are measured on cavity resonance. By solving Eq. (5) and Eq. (6) on the cavity resonance, we can obtain the mode matching efficiency η:

$$\eta = \frac{(1+\alpha)^2}{(2\alpha)^2} T(\omega_0) . \tag{8}$$

Similarly, the cavity decay rates are $\kappa_m = 2\kappa\alpha/(1+\alpha)$ and $\kappa_l = \kappa(1-\alpha)/(1+\alpha)$.

2.3. Beam shaping with SLM

A spatial filter which transforms one optical mode to another can be described by a generalized filter function $T(\mathbf{x}) = M(\mathbf{x}) \exp(i\,\Phi(\mathbf{x}))$ which modulates both the amplitude and the phase of the incoming mode. However, liquid crystal SLM only modulates the phase of the incoming beam and hence only provides the transformation $T(\mathbf{x}) = \exp(i\,\Phi(\mathbf{x}))$. To modulate the amplitude of the incoming beam as well, SLM can be operated in a phase-grating configuration – this produces both the carrier and first-order diffraction beams, which amplitude can be varied by the modulation depth [29, 30]. This method typically requires a high-resolution SLM to sufficiently encode the desired beam profile on the phase-grating, however recent works explored other encoding techniques which allows for amplitude modulation using low-resolution SLMs [25, 31–33]. Alternatively, using two SLMs and a polarizer allows to modulate the amplitude and phase of the incoming beam independently [34–36].

To generate LG modes necessary for cavity mode-matching from a collimated Gaussian beam, we utilize a much simpler technique [37–39] which spatially modulates the incoming Gaussian beam with the phase component of the desired LG modes. The SLM phase function is given by

$$\Phi(\rho, \phi) = \arg\left[U_{m,l}(\rho, \phi, 0)\right] = \arg\left[\mathcal{L}_m^l\left(\frac{2\rho^2}{w^2}\right)\right] - l\phi \tag{9}$$

with the incoming Gaussian mode $U_0(\rho) = A_0 \exp\left(-\rho^2/w_0^2\right)$. The ratio w/w_0 can be varied to optimize the mode overlap of the resulting SLM output mode to the particular LG mode – for

relatively small m and l mode numbers, the mode overlap is relatively high with low cross-mode overlap (see Table 1). The mode overlap is defined as the dot product between the two mode profiles $\int (d\sigma) U_1(\rho, \phi) U_2(\rho, \phi)$. The modulus square of mode overlap is the mode matching efficiency η as defined in Section 2.2.

Due to its simplicity, this technique is often implemented using physical phase plates [40, 41]. By subjecting the resulting beam to the cavity, only the resonant LG mode is transmitted while other LG modes with different resonance frequencies (see Eq. 2) are attenuated by the cavity.

		Mode matching efficiencies					
SLM output	W/W_0	LG_{00}	LG_{10}	LG_{20}	LG_{30}	LG_{40}	LG_{50}
LG_{10}	0.57	0.1%	**81.2%**	0.0%	2.4%	1.3%	0.7%
LG_{20}	0.45	1.3%	0.1%	**76.9%**	0.1%	1.6%	4.5%
LG_{30}	0.39	0.4%	1.2%	0.5%	**74.6%**	0.3%	0.9%
LG_{40}	0.35	0.2%	0.4%	1.2%	0.8%	**73.2%**	0.5%

Table 1. Calculated values of the mode matching efficiencies (the square of the mode overlap) between the SLM output and the LG modes for $l = 0$ cases, up to LG_{50}. The mode matching to the remaining higher order LG modes are small, and the total mode matching efficiencies sum up to unity.

3. Experiment

3.1. Experimental setup

The design and construction of the near-concentric cavity is described in previous works [20, 23]. The anaclastic lens-mirror design allows highly divergent modes of the near-concentric cavity to be transformed into collimated modes. This simplifies the requirement of the optical components to generate and measure collimated LG beams on the input and output of the cavity (see Figure 1).

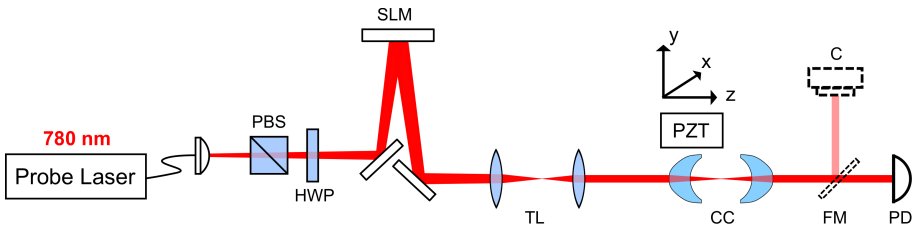

Fig. 1. Optical setup. The SLM (Meadowlark HV 512 DVI) transforms the probe light from the fiber output to match the LG modes of the near concentric cavity (CC). A telescope (TL) is introduced to facilitate mode matching between the SLM beam output and the cavity. The cavity transmission is monitored using either a photodetector (PD) or camera (C), set by the flip mirror (FM).

3.1.1. Mode Generation

As the SLM only modulates light with a particular linear polarization, a sequence of a polarizing beam-splitter (PBS) and a half-wave plate (HWP) prepares the correct polarization to match the SLM polarization axis. Considering the SLM resolution of 512x512 pixels, we minimize the pixelation artifact by using a significant portion of the SLM area (12.8 × 12.8 cm). To achieve

this, we prepare a slightly divergent beam with beam diameter ($1/e^2$ width) ranging from 3 to 7 mm, measured at the SLM.

The phase modulation applied on the SLM consists of three components: the LG mode-generating phase pattern as described in Eq. 9, the correction phase pattern provided by the manufacturer, and a quadratic phase pattern which effectively acts as a Fresnel lens with variable focal length. This SLM-generated Fresnel lens helps in filtering out the unmodulated light on the SLM output (more commonly done with a blazed grating pattern [39]). In addition, the combination of the Fresnel lens with a telescope of variable length and magnification creates a collimated LG beam with tunable beam size. The appropriate values for the Fresnel lens and telescope parameters are obtained with ray-tracing simulations.

3.1.2. Cavity Alignment

In the cavity design [23], one cavity mirror is placed on 3D piezo translation stage (Figure 1) to allow for both the longitudinal (z direction) and transverse alignment (x and y directions). The longitudinal alignment changes the cavity length to be resonant to a particular light frequency. The transverse alignment is necessary to bring the two mirrors to be cylindrically symmetric. Small rotational misalignment on the tip and tilt direction can also be corrected by the transverse alignment, if the mirrors are perfectly spherical. However, this correction might lead to the two anaclastic lens-mirror axes not exactly being aligned with the cavity axis, resulting in slightly asymmetric collimated output modes.

The transmission and reflection spectrum of the cavity are obtained by measuring the light intensity with a photodetector while varying the cavity length linearly over time. The detuning from the cavity resonance is expressed correspondingly in units of light frequency – the conversion factor can be determined by measuring the spacing of the frequency sideband generated with an electro-optical modulator. As the cavity is located inside a glass cuvette of the vacuum chamber, we characterize the cuvette transmission loss and apply the correction on the cavity spectra.

3.1.3. Measurement of the Mode Matching Efficiency

The mode matching efficiency η (Eq. 8) quantifies how well the input mode matches and couples to the cavity mode. It only depends on the power transmission at resonance $T(\omega_0)$ and the "effective" transmission coefficient α (Eq. 7). Nominally, $\alpha = \kappa_m/(2\kappa_l + \kappa_m)$ only depends on the ratio of the decay rates κ_m and κ_l, and thus is a physical property of the cavity mirrors.

We characterize the value of the α by coupling a Gaussian beam (from an aspheric-collimated single mode fiber output mode) into the cavity without the SLM. The transmission and reflection spectrum were recorded, and from the fitting, we obtained $T(\omega_0) = 19.5(1)\%$, $R(\omega_0) = 33.6(2)\%$, and $\kappa = 2\pi \times 24.8(8)\,\mathrm{MHz}$. From the fitted parameters, we estimated $\alpha = 0.294(2)$, which results in a mode matching efficiency of $\eta = 94(1)\%$ for Gaussian beam, and cavity decay rates of $\kappa_m = 2\pi \times 11.3(4)\,\mathrm{MHz}$ and $\kappa_l = 2\pi \times 13.5(4)\,\mathrm{MHz}$.

To estimate the mode matching efficiencies for SLM-generated LG modes, we obtain the cavity transmission spectrum $T(\omega)$ and multiply it with $(1+\alpha)^2/(2\alpha)^2$ (the prefactor in Eq. 8) to obtain the mode transmission spectrum $\eta(\omega)$. We fit this spectrum with a Lorentzian profile, and estimate the mode matching efficiency $\eta = \eta(\omega_0)$ from the fit amplitude. The parameters from the ray-tracing simulation helps to start the coupling procedure, and we fine-tune these values further to maximize the mode matching efficiency.

3.2. Mode-matching to single LG modes

We generate a single LG mode using the SLM and couple it to the near concentric cavity. The cavity is located at a critical distance of $d = 4.8(2)\mu\mathrm{m}$ with $g = -0.99912(4)$, corresponding to a measured transverse mode spacing of $\Delta\nu_{tr} = \nu_F(1 - \Delta\zeta/\pi) = 182(5)\,\mathrm{MHz}$ between adjacent LG modes. The cavity spectra and the camera-captured output modes are depicted on Figure 2

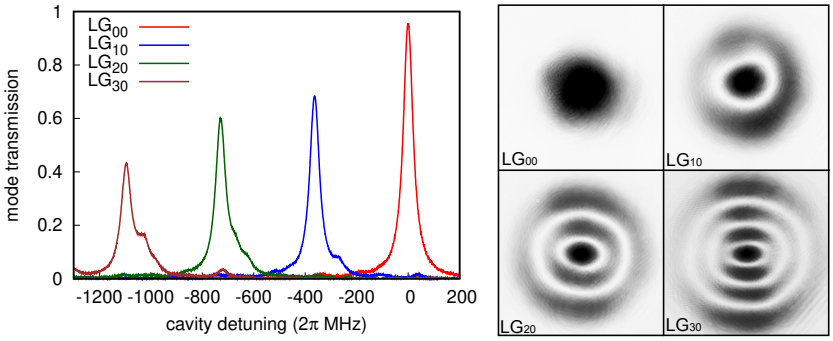

Fig. 2. Left: cavity mode transmission spectra of LG modes with no angular momentum ($l = 0$). The detuning is defined with respect to the LG_{00} resonance, and the modes are spaced $2\Delta\nu_{tr}$ apart. Right: the corresponding cavity mode output observed with the camera.

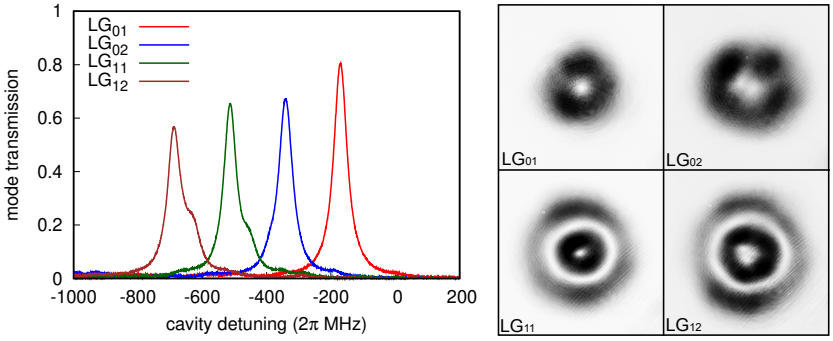

Fig. 3. Left: cavity mode transmission spectra of LG modes with a few units of angular momentum ($l = 1$ and $l = 2$). Right: the corresponding cavity mode output observed with the camera.

Mode	Sim.	Exp.
LG_{00}	100%	96(1)%
LG_{10}	81.2%	68(1)%
LG_{20}	76.9%	57(1)%
LG_{30}	74.7%	38(1)%

Mode	Sim.	Exp.
LG_{01}	93.1%	81(1)%
LG_{02}	84.4%	67(1)%
LG_{11}	81.8%	63(1)%
LG_{12}	79.8%	53(1)%

Table 2. Comparison of mode matching efficiencies between the simulation and the experiment for single LG modes.

for LG modes with no angular momentum ($l = 0$), and on Figure 3 for LG modes with angular momentum ($l \neq 0$). The measured mode matching efficiencies are close to the simulated values (see Table 2), although it degrades with higher mode numbers. We attribute this to limited SLM pixel resolution, axial mismatch between the cavity and the anaclastic lens axis due to the tip-tilt misalignment, and mirror surface deviation from a perfect spherical profile. These factors also contribute to some irregularities on the output mode observed by the camera.

3.3. Mode-matching to a superposition of LG modes

We demonstrate the coupling of the SLM-generated beam to an arbitrary superposition of LG modes. We use the method described in Section 3.1.1, by considering the resultant mode as a superposition of individual LG modes:

$$U_{res} = \sum A_{l,m} \exp\left(i\phi_{l,m}\right) LG_{lm}\,, \tag{10}$$

where $A_{l,m}$ is the amplitude of each constituting LG mode and $\phi_{l,m}$ is the relative phase of the LG mode.

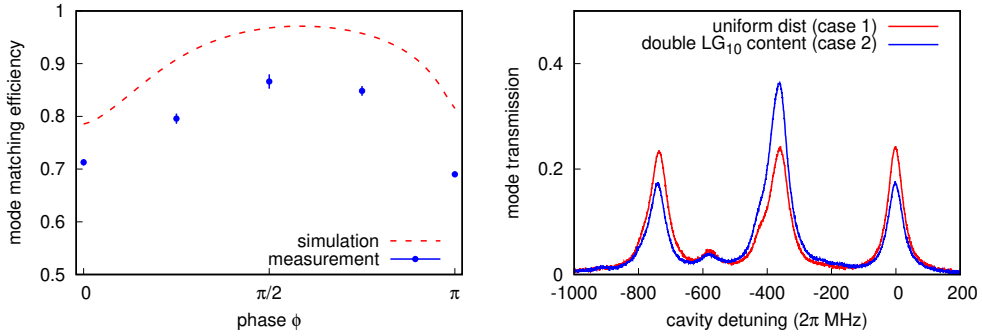

Fig. 4. Left: Coupling to equal parts of LG_{00} and LG_{10} modes while varying their phase difference. Right: Coupling to a superposition of LG_{00}, LG_{10} and LG_{20} modes.

Figure 4 (left) shows the mode matching efficiency in coupling the superposed mode $U_{\{00,10\}} = \left(LG_{00} + e^{i\phi} LG_{10}\right)/\sqrt{2}$ with varying relative phase angle ϕ. To obtain a balanced distribution of LG_{00} and LG_{10}, we introduce a mode amplitude A_{10} to the SLM spatial phase pattern:

$$\Phi = \arg\left[U_{\{00,10\}}\right] = \arg\left[\frac{LG_{00} + A_{10}e^{i\phi} LG_{10}}{\sqrt{1 + A_{10}^2}}\right], \tag{11}$$

and vary the amplitude A_{10} and w/w_0, maximising the mode matching efficiency subject to the balanced distribution constraint. The mode matching efficiency is obtained by adding the mode transmission amplitudes of both the LG_{00} and LG_{10} modes, while ensuring that they are balanced up to $\sim 1\%$ error. The measured values follow a similar trend with the simulated values, with some offset ($\sim 10\%$) attributable to the SLM pixel size and the mirror irregularities as described previously. The highest mode matching efficiency occurs around $\phi = \pi/2$, as the SLM encodes the LG_{00} and LG_{10} modes into the in-phase and quadrature component of the mode and increases its efficiency.

Figure 4 (right) shows the mode transmission spectra of a superposition of three modes. The modes LG_{00}, LG_{10}, and LG_{20} are superposed with a phase difference of $2\pi/3$ between each

mode, as to distribute the phases evenly on the complex plane. The SLM spatial pattern is given by:

$$\Phi = \arg\left[U_{\{00,10,20\}}\right] = \arg\left[\frac{LG_{00} + A_{10}e^{i2\pi/3}LG_{10} + A_{20}e^{i4\pi/3}LG_{20}}{\sqrt{1 + A_{10}^2 + A_{20}^2}}\right] \tag{12}$$

where A_{10}, A_{20} and w/w_0 are parameters to be varied to obtain the desired mode distribution and the efficiency. Two examples are illustrated in the figure: (1) equally distributed modes, i.e. $U_{\{00,10,20\}} = \left(LG_{00} + e^{i2\pi/3}LG_{10} + e^{i4\pi/3}LG_{20}\right)/\sqrt{3}$, and (2) LG_{10} content double the content of the other modes, i.e. $U_{\{00,10,20\}} = \left(LG_{00} + \sqrt{2}e^{i2\pi/3}LG_{10} + e^{i4\pi/3}LG_{20}\right)/2$. The theoretically calculated efficiencies under optimized parameters are 95.6% and 97.2% for case (1) and (2), while the measured efficiencies are 71(1)% and 70(1)%, respectively.

3.4. Mode-matching at different critical distances

The critical distance $d = 2R - L$ characterizes how far the cavity is away from the concentric configuration ($L = 2R$). Small critical distances provide strong field focusing and a small mode volume. In addition, the frequency spacing of the transverse modes decreases with smaller critical distances, leading to the mode degeneracy at the critical point [23].

We study how the mode matching of a single LG mode performs at different critical distances. We use the SLM to couple to LG_{00}, LG_{10}, and LG_{20} modes of the cavity, and obtain the cavity transmission spectra. We observe that the linewidth of the cavity spectra increases for smaller critical distances, while the mode transmission decreases. This is due to the diffraction losses as the cavity approaches the critical point.

The critical distance can be estimated from the transverse mode spacing. By changing the cavity length and keeping the laser frequency fixed, we obtain neighbouring cavity spectra spaced $\Delta d = \lambda/2$ apart. Figure 5 shows the amplitudes of the mode transmission and the cavity linewidths for various critical distances. For the case of no diffraction loss, the mode transmission amplitude is equivalent to the mode-matching efficiency η. However, as the diffraction loss increases, the "effective" cavity transmission α also changes. Hence, the mode transmission amplitude describes the mode-matching efficiency weighted by a factor associated with the diffraction loss. In the high diffraction loss regime, it becomes hard to couple to a particular lossy eigenmode, and characterize its linewidth to obtain α, as the modes start to overlap in frequency. Figure 6 shows the spatial profile of the cavity transmission mode, captured with the camera. The diffraction rings become visible at the critical distance where the linewidth increases.

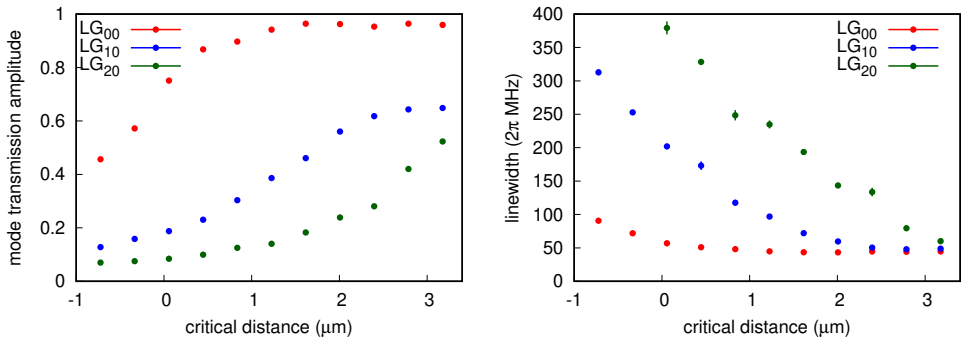

Fig. 5. Left: Mode transmission amplitude of different LG modes over a range of critical distances. Right: The corresponding linewidth (FWHM) of the modes.

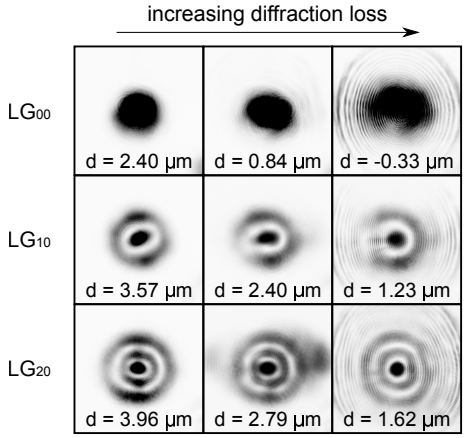

Fig. 6. The cavity modes observed with the camera, before and after the diffraction losses dominate. The diffraction rings are due to the aperture of the anaclastic lens.

The near-concentric cavity can support LG modes reasonably close (~ a few μm) to the critical point. However, higher order LG modes start to exhibit diffraction losses at larger critical distances, due to larger LG beam sizes. The performance of the cavity mirrors can be characterized with an effective aperture – for every round trip, the cavity mode bounces off a circular aperture with diameter a on the mirror, effectively blocking some outer parts of the beam. As a first order approximation, we assume the LG modes to be unperturbed after subsequent round trips. To estimate the onset of the diffraction loss, we choose an aperture size to block $\sim 1\%$ of the mode (the diffraction loss is $2\kappa_{ap} \sim 2\pi \times 20\,\mathrm{MHz}$), which on the same order as the mirror transmission and scattering losses. From Figure 5 (right), the effective aperture diameter is estimated to be $a_{\mathrm{exp}} = 1.40(6)\,\mathrm{mm}$ with the onset of the diffraction loss at critical distances of $0.46(8)\,\mu$m for LG_{00}, $1.8(3)\,\mu$m for LG_{10}, and $3.8(6)\,\mu$m for LG_{20}.

The estimated effective aperture $a_{\mathrm{exp}} = 1.40(6)\,\mathrm{mm}$ is comparatively lower than the nominal aperture of the anaclastic lens-mirror design $a_{\mathrm{nom}} = 4.07\,\mathrm{mm}$. We suspect this to be due to a combination of the following factors: (1) local aberrations of the mirror surface due to thermo-mechanical stresses [42, 43] and optical surface irregularities, (2) angle-dependent variation on the wavefront due to the multi-layered coating [44], as the deposition process creates thicker layers near the center of the mirror and thinner layers near the perimeter, (3) the validity of the paraxial approximation [45] for strongly diverging modes, particularly for higher orders. Even though the LG modes are quite far from degeneracy (~ 100 MHz) in this regime, it may be possible to reach near-degeneracy either by slightly modifying the mirror shape or the coating layers – this strategy would create a slightly different "effective" cavity length for different LG modes, allowing the modes to come closer or even overlap in frequency.

4. Conclusion

In summary, we have developed a mode-matching procedure for the transverse modes of a near-concentric cavity. Using an SLM, we engineer the spatial phase information of an input Gaussian beam to selectively mode-match with a specific LG mode, and achieve relatively high efficiencies for several low-order LG modes. Next, we demonstrate that an arbitrary superposition of cavity modes can be generated with a relatively high fidelity, limited by the resolution of the SLM device and the imperfections of cavity mirror surfaces. We show that the near-concentric cavity can support several LG modes up to critical distances of a few μm before the diffraction loss dominates. These results provide a valuable building block to explore strong interaction

betweens atoms and multi-mode photons in near-concentric cavities.

Funding

National Research Foundation, Prime Minister's office (partly under grant No. NRF-CRP12-2013-03).

References

1. J. Wang, J.-Y. Yang, I. M. Fazal, N. Ahmed, Y. Yan, H. Huang, Y. Ren, Y. Yue, S. Dolinar, M. Tur *et al.*, "Terabit free-space data transmission employing orbital angular momentum multiplexing," Nat. Photonics **6**, 488 (2012).
2. N. Bozinovic, Y. Yue, Y. Ren, M. Tur, P. Kristensen, H. Huang, A. E. Willner, and S. Ramachandran, "Terabit-scale orbital angular momentum mode division multiplexing in fibers," Science **340**, 1545–1548 (2013).
3. L. Zhu, J. Liu, Q. Mo, C. Du, and J. Wang, "Encoding/decoding using superpositions of spatial modes for image transfer in km-scale few-mode fiber," Opt. Express **24**, 16934–16944 (2016).
4. A. Hasnaoui, A. Bencheikh, M. Fromager, E. Cagniot, and K. Aït-Ameur, "Creation of a sharper focus by using a rectified temp0 beam," Opt. Commun. **284**, 1331–1334 (2011).
5. M. Mafu, A. Dudley, S. Goyal, D. Giovannini, M. McLaren, M. J. Padgett, T. Konrad, F. Petruccione, N. Lütkenhaus, and A. Forbes, "Higher-dimensional orbital-angular-momentum-based quantum key distribution with mutually unbiased bases," Phys. Rev. A **88**, 032305 (2013).
6. R. Fickler, R. Lapkiewicz, W. N. Plick, M. Krenn, C. Schaeff, S. Ramelow, and A. Zeilinger, "Quantum entanglement of high angular momenta," Science **338**, 640–643 (2012).
7. P. Horak, H. Ritsch, T. Fischer, P. Maunz, T. Puppe, P. W. Pinkse, and G. Rempe, "Optical kaleidoscope using a single atom," Phys. Rev. Lett. **88**, 043601 (2002).
8. P. Maunz, T. Puppe, T. Fischer, P. W. Pinkse, and G. Rempe, "Emission pattern of an atomic dipole in a high-finesse optical cavity," Opt. Lett. **28**, 46–48 (2003).
9. T. Puppe, P. Maunz, T. Fischer, P. W. Pinkse, and G. Rempe, "Single-atom trajectories in higher-order transverse modes of a high-finesse optical cavity," Phys. Scripta **2004**, 7 (2004).
10. T. Klaassen, J. de Jong, M. van Exter, and J. Woerdman, "Transverse mode coupling in an optical resonator," Opt. Lett. **30**, 1959–1961 (2005).
11. J. Benedikter, T. Hümmer, M. Mader, B. Schlederer, J. Reichel, T. W. Hänsch, and D. Hunger, "Transverse-mode coupling and diffraction loss in tunable fabry–pérot microcavities," New J. Phys. **17**, 053051 (2015).
12. M. Gangl, P. Horak, and H. Ritsch, "Cooling neutral particles in multimode cavities without spontaneous emission," J. Mod. Opt. **47**, 2741–2753 (2000).
13. H. Ritsch, P. Domokos, F. Brennecke, and T. Esslinger, "Cold atoms in cavity-generated dynamical optical potentials," Rev. Mod. Phys. **85**, 553 (2013).
14. A. T. Black, H. W. Chan, and V. Vuletić, "Observation of collective friction forces due to spatial self-organization of atoms: from rayleigh to bragg scattering," Phys. Rev. Lett. **91**, 203001 (2003).
15. S. Gopalakrishnan, B. L. Lev, and P. M. Goldbart, "Emergent crystallinity and frustration with bose–einstein condensates in multimode cavities," Nat. Phys. **5**, 845–850 (2009).
16. A. J. Kollár, A. T. Papageorge, K. Baumann, M. A. Armen, and B. L. Lev, "An adjustable-length cavity and bose–einstein condensate apparatus for multimode cavity qed," New J. Phys. **17**, 043012 (2015).
17. V. D. Vaidya, Y. Guo, R. M. Kroeze, K. E. Ballantine, A. J. Kollár, J. Keeling, and B. L. Lev, "Tunable-range, photon-mediated atomic interactions in multimode cavity qed," Phys. Rev. X **8**, 011002 (2018).
18. Y. Guo, R. M. Kroeze, V. D. Vaidya, J. Keeling, and B. L. Lev, "Sign-changing photon-mediated atom interactions in multimode cavity quantum electrodynamics," Phys. Rev. Lett. **122**, 193601 (2019).
19. S. Morin, C. Yu, and T. Mossberg, "Strong atom-cavity coupling over large volumes and the observation of subnatural intracavity atomic linewidths," Phys. Rev. Lett. **73**, 1489 (1994).
20. K. Durak, C. H. Nguyen, V. Leong, S. Straupe, and C. Kurtsiefer, "Diffraction-limited fabry–perot cavity in the near concentric regime," New J. Phys. **16**, 103002 (2014).
21. C. H. Nguyen, A. N. Utama, N. Lewty, K. Durak, G. Maslennikov, S. Straupe, M. Steiner, and C. Kurtsiefer, "Single atoms coupled to a near-concentric cavity," Phys. Rev. A **96**, 031802 (2017).
22. A. T. Papageorge, A. J. Kollár, and B. L. Lev, "Coupling to modes of a near-confocal optical resonator using a digital light modulator," Opt. Express **24**, 11447–11457 (2016).
23. C. H. Nguyen, A. N. Utama, N. Lewty, and C. Kurtsiefer, "Operating a near-concentric cavity at the last stable resonance," Phys. Rev. A **98**, 063833 (2018).
24. C. Hamsen, K. N. Tolazzi, T. Wilk, and G. Rempe, "Strong coupling between photons of two light fields mediated by one atom," Nat. Phys. **14**, 885–889 (2018).
25. A. Forbes, A. Dudley, and M. McLaren, "Creation and detection of optical modes with spatial light modulators," Adv. Opt. Photonics **8**, 200–227 (2016).
26. F. Dubois, P. Emplit, and O. Hugon, "Selective mode excitation in graded-index multimode fiber by a computer-generated optical mask," Opt. Lett. **19**, 433–435 (1994).
27. B. E. A. Saleh and M. C. Teich, *Resonator Optics* (John Wiley & Sons, Inc., 2001), pp. 310–341.

28. C. J. Hood, H. J. Kimble, and J. Ye, "Characterization of high-finesse mirrors: Loss, phase shifts, and mode structure in an optical cavity," Phys. Rev. A **64**, 033804 (2001).
29. J. P. Kirk and A. L. Jones, "Phase-only complex-valued spatial filter," JOSA **61**, 1023–1028 (1971).
30. J. A. Davis, D. M. Cottrell, J. Campos, M. J. Yzuel, and I. Moreno, "Encoding amplitude information onto phase-only filters," Appl. Opt. **38**, 5004–5013 (1999).
31. V. Arrizón, U. Ruiz, R. Carrada, and L. A. González, "Pixelated phase computer holograms for the accurate encoding of scalar complex fields," JOSA A **24**, 3500–3507 (2007).
32. T. Ando, Y. Ohtake, N. Matsumoto, T. Inoue, and N. Fukuchi, "Mode purities of laguerre–gaussian beams generated via complex-amplitude modulation using phase-only spatial light modulators," Opt. Lett. **34**, 34–36 (2009).
33. T. W. Clark, R. F. Offer, S. Franke-Arnold, A. S. Arnold, and N. Radwell, "Comparison of beam generation techniques using a phase only spatial light modulator," Opt. Express **24**, 6249–6264 (2016).
34. R. D. Juday and J. M. Florence, "Full-complex modulation with two one-parameter slms," in *Wave Propagation and Scattering in Varied Media II,* vol. 1558 (International Society for Optics and Photonics, 1991), pp. 499–504.
35. L. G. Neto, D. Roberge, and Y. Sheng, "Full-range, continuous, complex modulation by the use of two coupled-mode liquid-crystal televisions," Appl. Opt. **35**, 4567–4576 (1996).
36. S. Reichelt, R. Häussler, G. Fütterer, N. Leister, H. Kato, N. Usukura, and Y. Kanbayashi, "Full-range, complex spatial light modulator for real-time holography," Opt. Lett. **37**, 1955–1957 (2012).
37. J. Arlt, K. Dholakia, L. Allen, and M. Padgett, "The production of multiringed laguerre–gaussian modes by computer-generated holograms," J. Mod. Opt. **45**, 1231–1237 (1998).
38. Y. Ohtake, T. Ando, N. Fukuchi, N. Matsumoto, H. Ito, and T. Hara, "Universal generation of higher-order multiringed laguerre-gaussian beams by using a spatial light modulator," Opt. Lett. **32**, 1411–1413 (2007).
39. N. Matsumoto, T. Ando, T. Inoue, Y. Ohtake, N. Fukuchi, and T. Hara, "Generation of high-quality higher-order laguerre-gaussian beams using liquid-crystal-on-silicon spatial light modulators," JOSA A **25**, 1642–1651 (2008).
40. K. Sueda, G. Miyaji, N. Miyanaga, and M. Nakatsuka, "Laguerre-gaussian beam generated with a multilevel spiral phase plate for high intensity laser pulses," Opt. Express **12**, 3548–3553 (2004).
41. A. Bencheikh, M. Fromager, and K. A. Ameur, "Generation of laguerre–gaussian lg p0 beams using binary phase diffractive optical elements," Appl. Opt. **53**, 4761–4767 (2014).
42. T. Legero, T. Kessler, and U. Sterr, "Tuning the thermal expansion properties of optical reference cavities with fused silica mirrors," JOSA B **27**, 914–919 (2010).
43. P. R. Yoder, *Mounting optics in optical instruments*, vol. 2 (SPIE press, 2008).
44. D. Kleckner, W. T. Irvine, S. S. Oemrawsingh, and D. Bouwmeester, "Diffraction-limited high-finesse optical cavities," Phys. Rev. A **81**, 043814 (2010).
45. C. G. Chen, P. T. Konkola, J. Ferrera, R. K. Heilmann, and M. L. Schattenburg, "Analyses of vector gaussian beam propagation and the validity of paraxial and spherical approximations," JOSA A **19**, 404–412 (2002).